IEEE Robotics and Automation Letters (RA-L) paper, presented at ICRA 2026, Vienna, Austria. Cite as RA-L paper.

# Design and Modeling of a Reconfigurable Robot: Decoupled STAR (DSTAR)

Tomer Siboni[1], Matan Coronel[1], and David Zarrouk[1]

***Abstract*— This paper presents Decoupled STAR (DSTAR), a novel reconfigurable robot fitted with a sprawling mechanism that allows the wheel rotation axes to vary relative to the body, and two independently activated four-bar extension mechanisms (FBEM). These mechanisms enable the robot to move its center of mass (COM) in any direction, and increase its maneuvering capabilities by selecting a variety of locomotion gaits. A kinematic model of the robot and a quasi-static force analysis are used to optimize the design and evaluate its motor requirements. Experiments demonstrate that combining the sprawling mechanism with FBEM enables the DSTAR to both crawl and drive, overcome a wide range of challenging obstacles, and improve its climbing capability by 66% compared to symmetric FBEM designs (such as RSTAR). The robot can crawl and maneuver over rough terrain using its unique turtle-gait method, roll sideways to surmount wall obstacles up to 20 cm high, travel horizontally across uneven ground, and switch between wheels and whegs to adapt to different terrain types, including dirt, stones, and grass. (see attached video).**

***Index Terms*— Field Robot, Reconfigurable Robot, Sprawl Tuning, Extension Mechanisms, Mechanical Design.**

## I. Introduction

Palm-sized crawling robots offer significant advantages for search and rescue operations, particularly in collapsed structures or rugged terrains. Their ability to traverse obstacles and access confined spaces enable safer and more efficient response efforts. Because they are lightweight and compact, these robots can be deployed in large swarms for rapid inspection. Today, several small robots can crawl at speeds exceeding multiple times their body length per second using bio-inspired designs that have demonstrated remarkable agility [1]-[6]. Although aerial systems such as drones have demonstrated advanced rescue capabilities [7]-[10], their effectiveness is limited in environments such as rubble-filled areas characterized by dust and unstructured terrains, and confined spaces such canals and pipes.

Miniature crawling robot designs can be enhanced by incorporating passive intelligent mechanics with models that only require a small number of motors. Large numbers of motors add weight, which impairs the robot's control and performance. Recent studies have explored different types of reconfigurable kinematics to enable these robots to traverse different terrains and overcome obstacles efficiently. These approaches include innovative mechanisms that allow the wheels to transform into legs or to adapt their shape [11]-[14], by employing dynamic locomotion strategies to shift the center of mass (COM) to enhance stability and agility in complex terrains [15]-[17]. By adjusting their COM, these robots can perform rolling motions, self-balance, and negotiate obstacles better [18]-[27].

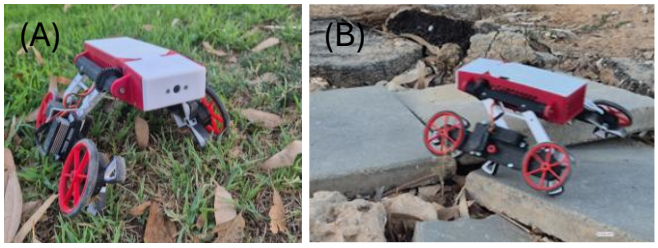


Figure 1. The DSTAR robot navigating an uneven terrain using its sprawl and FBEM mechanisms. **(**A**)** Crawling over grass. **(**B**)** Crawling over uneven surfaces and rubble. (See attached video).

The Decoupled STAR (DSTAR) is a successor in the "STAR" robot family, which includes several predecessors with distinct capabilities. The original STAR, designed for high-speed locomotion, featured a compact and lightweight design (73 g) [28] and reached speeds of up to 5 m/s. Its successor, the RSTAR [29], demonstrated a wide range of ground-based locomotion modes and obstacle engagement, including climbing over 6 cm step obstacles and performing the turtle gait, though without the ability to turn. The TSTAR [30], a larger robot also designed for obstacle negotiation, introduced unique climbing capabilities using a two-joint tail mechanism, enabling it to overcome obstacles up to 18 cm high, but it lacked the ability to perform the turtle gait. The Flying FSTAR and FCSTAR [31][32] expanded the family with both ground and aerial capabilities, allowing rapid traversal of slopes and walls, though without specialized obstacle engagement. Finally, the AmphiSTAR [33], designed for both terrestrial and aquatic operation, achieved high speeds of up to 3.5 m/s on land and 1.5 m/s in water with seamless transition between the two media, but it had limited obstacle-climbing capabilities.

Note that the simplicity of their design and their passive mechanics allow the STAR robots to adapt to diverse terrains and challenging environments. This design has also proved helpful in simplifying teaching the robots "obstacle engagement" (with deep reinforcement learning [34]) to improve performance, while minimizing energy consumption or task duration.

The DSTAR, designed to overcome diverse obstacles, is an upscaled version (ratio of ~ 1.5:1) of the RSTAR with a reconfigurable design that incorporates two independent four-bar mechanisms, an extended sprawl range, and enhanced motor and control capabilities. These innovations enable the robot to perform tasks beyond RSTAR's capabilities, including stable omnidirectional navigation using the turtle gait (without reliance on wheels), sideways rolling to overcome large obstacles (such as 15 cm typical steps and 20 cm high wall obstacles), self-recovery from stuck situations, passage through vertical cracks, flipping over to change its contact wheels, and

This research was funded by the by the Helmsley Charitable Trust through the Agricultural, Biological and Cognitive Robotics Initiative and by the Marcus Endowment Fund both at Ben-Gurion University of the Negev.

T. Siboni, M. Coronel and D. Zarrouk are associated with the Department of Mechanical Engineering, Ben Gurion University of the Negev, Israel. (zadavid@bgu.ac.il).

even traveling sideways. Using an asymmetric FBEM configuration, the robot can cross an 18 cm horizontal gap.

This paper is organized as follows. The mechanical design of the robot is presented in Section II. Section III outlines the kinematics and work volume of the robot and provides a quasi-static force and torque analysis to determine the torque requirements of the motors and the conditions for driving and rolling over sideways under different conditions. Section IV present multiple experiments in which the robot rolls over sideways, crawls and turns using different dedicated gaits, and travels over different terrains.

## II. Design and Manufacturing

The primary design goal of the DSTAR robot was to develop a simple but highly adaptable and versatile robot that can navigate challenging terrains and overcome obstacles. The design needed to balance compactness and lightweight construction with the ability to reconfigure for maximum maneuverability while carrying essential payloads such as a micro-computer, a camera, and other sensors.

### A. Robot Design

The DSTAR robot is composed of a rigid body base (that houses its onboard power supplies, a Raspberry Pi, drivers, and a camera), a sprawl mechanism, and two FBEM mechanisms. Nearly 50% of the robot's mass is concentrated in the main body, with the leg structures on either side accounting for approximately 25% each. A servo motor located at the front of the body drives the sprawl mechanism, while each FBEM is powered by a separate servo motor, which increases its maneuverability and ability to adapt to a range of terrains.

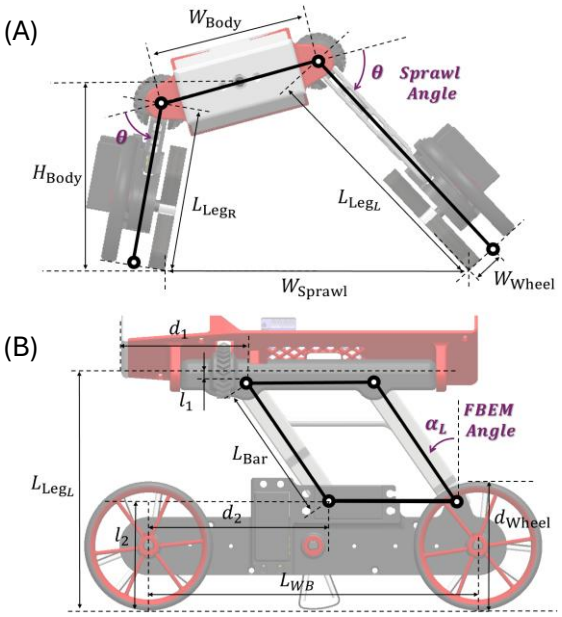


Figure 2. The mechanical design of the DSTAR robot. (A) Front view showing the sprawling mechanism. (B) Side view showing the left FBEM.

The robot's leg configurations are modular, enabling quick replacement with different wheel types or leg lengths based on mission needs. Each set of three wheels/whegs on each side is driven by a single motor.

#### 1) The Sprawl Mechanism

The sprawl mechanism enables the robot to symmetrically control the deviation of the wheels/legs axes relative to the body (Figure 2A). The sprawl angle $\theta$ is defined as 0° when the robot is "flat" (the wheel axes are perpendicular to the body). The sprawl can range from -105° to +105°, enabling upside-down driving and rolling maneuvers. The sprawl is actuated by a single servo motor. A 1:1 gear transmission is used to rotate the connectors holding the FBEM mechanisms on both sides.

#### 2) The Four-Bar Extension Mechanism (FBEM)

Each side of the robot has an independent FBEM that adjusts the wheels' distance from the body while keeping the legs parallel to the body. Together with the sprawl, they allow rolling maneuvers and enable a variety of gaits in confined spaces and over different surfaces. The FBEM angles $\alpha_L$ and $\alpha_R$ are defined as 0° when fully extended and vary within ±65° (Figure 2B). They have positive values when the robot is "leaning" forward. A custom connector integrates both mechanisms for smooth actuation and easy maintenance (Figure 3).

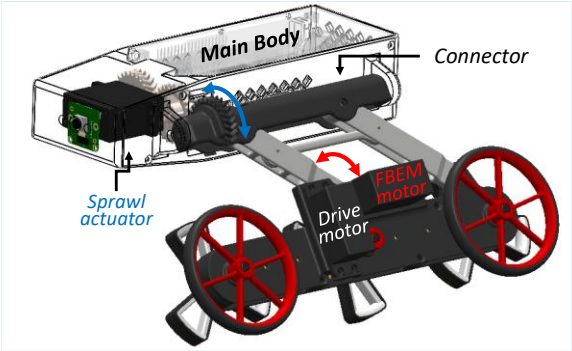


Figure 3. The FBEM mechanisms are attached to the sprawling mechanism using a connector. The sprawl is symmetric on both sides and is actuated using a single motor, whereas each FBEM is actuated using a separate motor. Two motors, one on each side, drive the wheels/whegs.

### B. Actuation and Control

The robot uses digital servo motors for reconfiguration and drive. The sprawl mechanism is powered by a 9imod DSC55MG servo (5.4 Nm, 750°/s at 8.4V), two NEEBRC NB-H015 servos actuate the FBEM (2.29 Nm, 333°/s at 6V) and two other servos SA19 drive the wheels (1.77 Nm, 105 RPM at 6V).

The robot is controlled using a Raspberry Pi 4 B and an Auto pHat driver and is powered by a 2-cell LiPo battery (7.8–8.4V). Voltage regulators are used to provide the nominal tension required for the electronic components. A second, smaller battery is used to power the onboard computing system.

For communication, the robot is equipped with both Wi-Fi and Bluetooth, allowing it to interface wirelessly with external devices or networks during operation. The robot can be driven either by direct remote control or programmed to automatically perform preplanned maneuvers.

### C. Manufacturing

Most parts were 3D printed using PLA+ on a Bamboo Lab X1 printer. A 0.2 mm layer height was used for large components, whereas critical parts like the wheel shafts were printed at 0.08 mm for strength and precision. One key focus

during the design process was to simplify part replacement. Most parts can be swapped out within a few minutes. The final design demonstrated high reliability, with no failures observed during extensive testing.

## III. Kinematic and Force Analysis

This section analyzes the DSTAR's kinematics, force, and torque requirements using robot parameters (TABLE I. ), guiding design validation and motor selection. Note that in parts A to C we used coordinate system "**O**" and in parts D and E we used coordinate systems "**A**" or "**A'**".

TABLE I. The parameters of the actual robot used in the kinematic and force analyses

| Description | Symbol | Value | Units |
|---|---|---|---|
| Robot Mass | $m$ | 1150 | $g$ |
| Body Mass | $m_{\text{Body}}$ | 590 | $g$ |
| Leg Mass | $m_{\text{Leg}}$ | 280 | $g$ |
| Bar Length | $L_{\text{Bar}}$ | 85 | $mm$ |
| Body Width | $W_{\text{Body}}$ | 96 | $mm$ |
| Body Length | $L_{\text{Body}}$ | 217 | $mm$ |
| Wheel Width | $W_{\text{Wheel}}$ | 20 | $mm$ |
| Wheel/Wheg Diameter | $d_{\text{Wheel}}$ | 76 | $mm$ |
| Sprawl angle [range] | $\theta$ | [-105,105] | $degree$ |
| Four- bar angle [range] | $\alpha_{R/L}$ | [-65,65] | $degree$ |
| Length of wheel base | $L_{WB}$ | 193 | $mm$ |
| Distance of top front FBEM axis from the robot's front | $d_1$ | 74 | $mm$ |
| Distance of bottom front FBEM axis from the front wheel's center | $d_2$ | 106 | $mm$ |
| Distance of top FBEM bar from the connector's axis | $l_1$ | 5 | $mm$ |
| Distance of bottom FBEM bar from the end of the leg | $l_2$ | 62 | $mm$ |

### A. Kinematic Analysis

We first calculated the position of the leg/wheel contact points (tips) with the surface relative to the center of the body (coordinate system "**O**") as a function of the sprawl and FBEM angles. Points **A–F** (Figure 4) define contact points as vectors relative to the frontal face of the body **O**. The primes mark the outer point of the wheel.

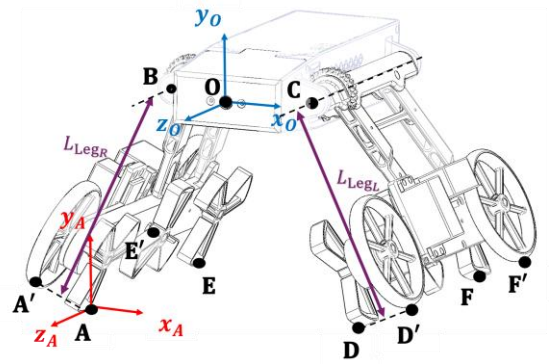


Figure 4. Contact points **A**, **D**, **E**, **F** used in the work volume analysis. The primes mark the outer point of the wheel. Coordinate system "**O**" is defined at point O, fixed to the robot body, while coordinate system "**A**" is defined at point A, fixed to the ground reference frame.

The length of the legs is:

$$L_{\text{Leg}_{R/L}} = l_1 + l_2 + L_{\text{Bar}} \cos\alpha_{R/L} \qquad (1).$$

Where "$R$" and "$L$" denote the right and left sides respectively. Given our robot parameters, the value of $L_{\text{Leg}}$ ranges from 103 to 153 mm (as a function of the FBEM angle $\alpha$). Please see Figure 2B.

The vector position of point A, representing the inner right front wheel's contact with the ground in reference system "**O**", is formulated as:

$$\mathbf{A} = \begin{pmatrix} \frac{-W_{\text{Body}}}{2} - L_{\text{Leg}_R}\cos\theta + W_{\text{Wheel}}\sin\theta \\ -L_{\text{Leg}_R}\sin\theta - W_{\text{Wheel}}\cos\theta \\ d_2 - d_1 - L_{\text{Bar}}\sin\alpha_R \end{pmatrix} \qquad (2).$$

The expressions for the other contact points (**A'**, **D**, **D'**) follow the same structure with simple substitutions for side and position. Point **A'** represents the outer right front wheel and is structurally identical to **A** except for the change in the sign of the wheel width term $W_{\text{Wheel}}$. Point **D** corresponds to the inner left front wheel, using $+W_{\text{Body}}/2$, the left leg length $L_{\text{LegL}}$, and the left FBEM angle $\alpha_L$. Point **D'** is the outer left front wheel and mirrors **D** with the wheel width term as a negative value.

Points **E'** and **F'** are the contact points of the rear wheels with the ground; hence, their locations in space are the same as **A'** and **D'** respectively, with a shift of $L_{\text{WB}}$ on the Z axis. Please see Figure 2 and Figure 4

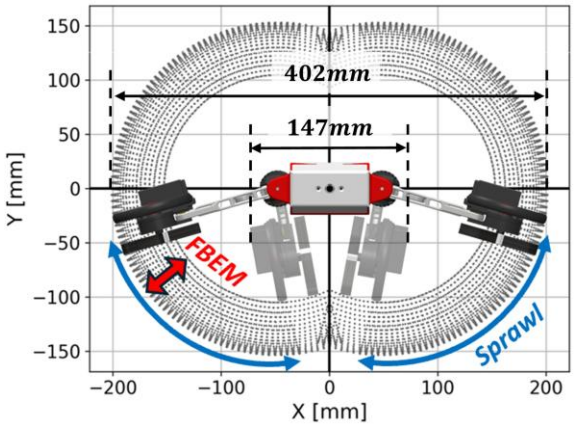


Figure 5. Front view of the "work volume" of the DSTAR legs, in "O" coordinate system.

### B. Advancing and Rotating using the Turtle Gait

The turtle gait enables effective locomotion across smooth terrain, dirt, and grass where wheels may dig in or become tangled and allows the robot to climb obstacles up to 9 cm high (Figure 6 and Section IV.A). This gait consists of moving the legs backward relative to the body ($\alpha=\alpha_B>0°$) when the sprawl is positive (legs touching the ground), which causes the body to move forward, and then moving the legs forward ($\alpha=\alpha_F<0°$) when the sprawl is negative (legs not touching the ground). In a single cycle, the expected forward (or backward) motion for a single turtle gait is:

$$d_{\text{Step}} = L_{\text{Bar}}\left(-\sin\alpha_F + \sin\alpha_B\right) \qquad (3).$$

Similarly, the robot can turn using the same technique but by reversing the sides of the legs; i.e., when the right leg moves to the front, the left leg moves to the back and vice-versa (Figure 7).

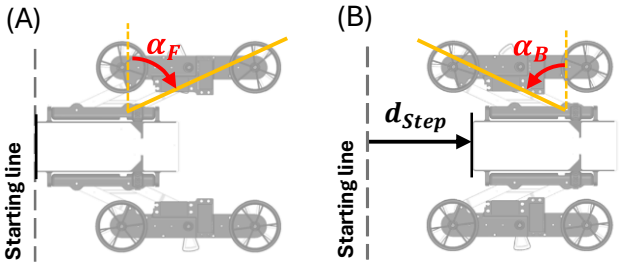


Figure 6. The distance a leg moves when changing the FBEM angles from $\alpha_F$ (A) to $\alpha_B$ (B).

Assuming symmetry in angle ranges and that the distance between the wheels (width direction) does not change, and the rear contact point in both legs does not slip, the rotation in each gait $\phi$ is:

$$\phi = \phi_F + \phi_B \tag{4},$$

where $\phi_F$ and $\phi_B$ are the contribution of $\alpha_F$ and $\alpha_B$ to the rotation and are:

$$\phi_{F/B} = atan\left(\frac{L_{\text{Bar}}\, sin|\alpha_{F/B}|}{\frac{W_{\text{Body}}}{2} + l_1 + l_2 + L_{\text{Bar}}\, cos|\alpha_{F/B}|}\right) \tag{5}.$$

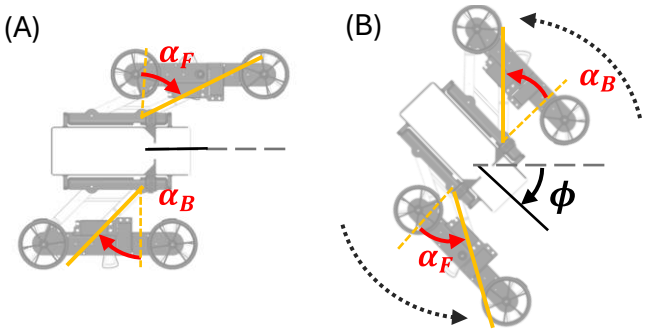


Figure 7. As the robot moves one leg forward and the other backward, the robot rotates by an angle of $\phi$.

### C. Contact Points with the Surface and Body Tilt

To determine the tilt angle of the robot's body, we assume that points **A** and **D** are in contact with the ground (as in Figure 8). Using reference system "**O**", the tilt angle $\gamma$ is given by:

$$\gamma = -atan\left(\frac{D_y - A_y}{D_x - A_x}\right) \tag{6}.$$

Once the tilt angle is defined, the conditions $\theta+\gamma<90°$ and $\theta-\gamma<90°$ need to be met. If not, $\gamma$ needs to be recalculated using **A'** and **D'** respectively.

Note that controlling the tilt allows the robot to keep its balance and maintain its body horizontal even when driving over a slope. Figure 9 presents the tilt of the robot as a function of the FBEM angle $\alpha_R$, while $\alpha_L$=0°, for different sprawl angles. Section III.D describes the conditions for rolling sideways.

### D. Mobility of the COM and Rolling Sideways

One of the unique capabilities of the DSTAR robot is its ability to control the position of its center of mass (COM) in all directions, thus allowing the robot to roll sideways using an asymmetric FBEM.

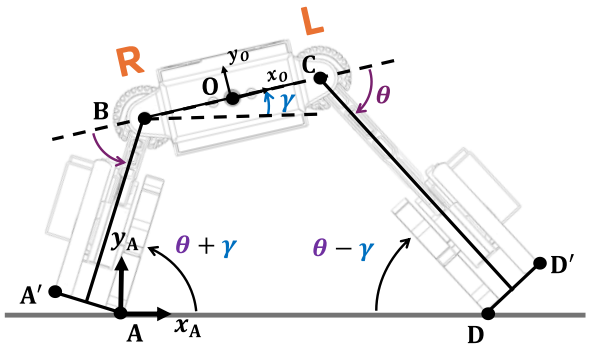


Figure 8. The robot shown leaning to the right. The angle $\gamma$ is the body's tilt (roll direction) relative to the surface.

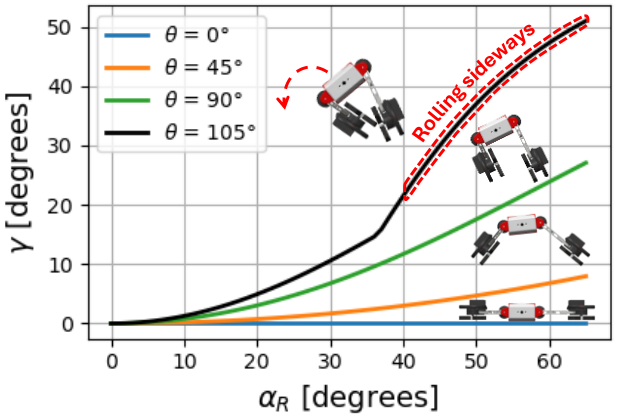


Figure 9. The tilt angle as a function of the FBEM angle $\alpha_R$, while $\alpha_L$=0° , for different sprawl angles. The dashed red line depicts the robot's ability to roll to the side on level ground.

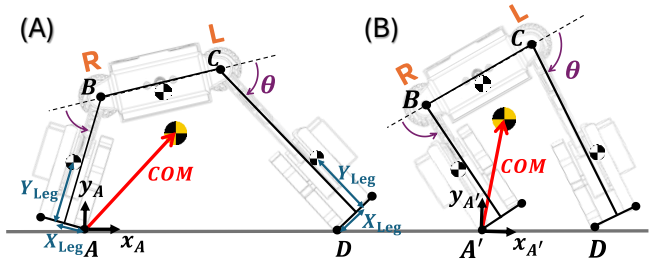


Figure 10. The location of the COM of the robot in the frontal plane. In (A) the contact point **A** is at the inner wheel/wheg, while in (B), the contact point **A'** is at the outer wheel.

The COM coordinates $\mathbf{X}_{\mathbf{COM}}$ are calculated in reference system "**A**" or "**A'**", depending on the wheels contact point, using:

$$\mathbf{X}_{COM} = \left(m_{\text{Body}}\mathbf{C}_{\text{Body}} + m_{\text{Leg}_R}\mathbf{C}_{\text{Leg}_R} + m_{\text{Leg}_L}\mathbf{C}_{\text{Leg}_L}\right)m^{-1} \tag{7}.$$

The values of the masses $m_{\text{Body}}$, $m_{\text{LegR}}$ and $m_{\text{LegL}}$ can be found in TABLE I. , and the vector positions $\mathbf{C}_{\text{Body}}$, $\mathbf{C}_{\text{LegR}}$ and $\mathbf{C}_{\text{LegL}}$ can be found in the Appendix.

Figure 11 presents the COM's position in the lateral ("$x$") direction as a function of the sprawl and right FBEM rotation $\alpha_R$ for $\alpha_L$=0°. If the value is negative ($\mathbf{X}_{\text{COMx}}$<0), the robot will roll sideways. As depicted, the minimum required sprawl and FBEM angles are respectively $\theta$>99° (for $\alpha_R$=65°) and $\alpha_R$=40°,

for ($\theta$=105°). The rolling zone (in red) occurs for high values of $\alpha$ and $\theta$.

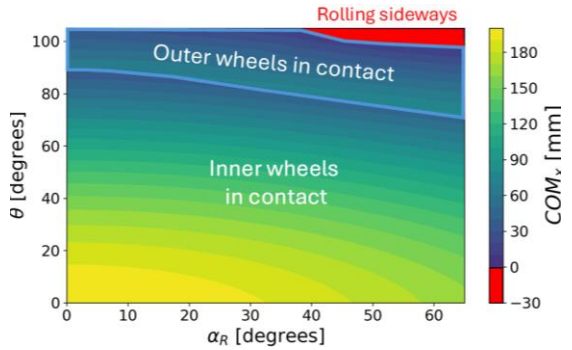


Figure 11. The shift of the robot's COM to the side through the coordinated use of the sprawl and FBEM with discontinuities reflecting the change in contact from the inner wheels to the outer wheels.

Note that the bar length critically determines DSTAR's flipping and climbing performance. Below 6.2 cm, sideways rolling is impossible (the red zone disappears), while at least 8.5 cm is required to climb a typical 15 cm stair ($L_{\text{Leg}}$=15 cm). Longer bars can enable higher obstacle climbing but at the cost of greater motor effort and increased robot size.

### *E. Force and Torque Quasi-static Analysis*

This section presents the calculations (using "**A**" or "**A'**" reference system) for the contact forces with the surface and the torque requirements of the sprawl and FBEM. It is assumed that the robot is leaning to the right, and that the values are symmetrical for the other side.

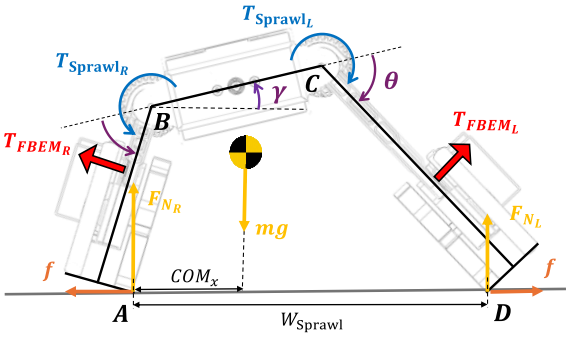


Figure 12. Frontal view of the contact forces and internal robot torques when the wheels are not actuated.

#### *1) Sprawl Torque Requirements*

Figure 12 illustrates the normal and frictional forces, denoted as $F_{N_{R/L}}$ and $f$, at points **A** and **D**. We assume a rightward lean and equal coefficient of friction (COF) on both sides, causing the left wheels to slide. The COF $\mu$ is taken as static at the onset of sliding, and kinetic during the sliding. The sprawl torque $T_{\text{Sprawl}}$ is generated by a single servo motor through a gear transmission actuating both sides. Given the FBEM asymmetry, the sprawl torque is calculated separately for each side as a function of angles $\theta$, $\alpha_R$, and $\alpha_L$, and then summed up. Assuming quasi-static motion, the COM's lateral position ($COM_x$) determines the weight distribution on each side. The normal forces are:

$$F_{N_R} = mg\left(1-\frac{COM_x}{W_{\text{Sprawl}}}\right), \qquad F_{N_L} = mg\frac{COM_x}{W_{\text{Sprawl}}} \tag{8}.$$

For a rightward lean $F_{NR}>F_{NL}$ (when the COM is closer to the right), the left side will slide when the sprawl and FBEM are actuated. The right side's frictional force balances the left side's horizontal friction force so that the frictional forces are:

$$f = \mu mg\frac{COM_x}{W_{\text{Sprawl}}} \tag{9}.$$

The sprawl torques that the robot applies are:

$$\left|T_{\text{Sprawl}_L}\right| = \left|(\mathbf{D}-\mathbf{C})\times(\mathbf{F}_{N_L}+\mathbf{f})\right| = \left|(D_x-C_x)F_{N_L}+C_y f\right| \tag{10}$$

$$\left|T_{\text{Sprawl}_R}\right| = \left|(\mathbf{A}-\mathbf{B})\times(\mathbf{F}_{N_R}+\mathbf{f})\right| = \left|B_x F_{N_R}+B_y f\right| \tag{11}.$$

Given that the sprawl is actuated by a single motor, the total torque acting on the motor is:

$$\left|T_{\text{Sprawl}}\right| = \left|T_{\text{Sprawl}_R}\right| + \left|T_{\text{Sprawl}_L}\right| \tag{12}$$

$$T_{\text{Sprawl}} = mg\left(\left((D_x-C_x)+(B_y+C_y)\mu\right)\frac{COM_x}{W_{\text{Sprawl}}}+B_x\left(1-\frac{COM_x}{W_{\text{Sprawl}}}\right)\right) \tag{13}.$$

Figure 13 illustrates sprawl torque as a function of the COF and the sprawl angle. The maximum expected load of 2.2 Nm (figure 12 A) is obtained when the legs are extended ($\alpha$=0°). The torques decrease by up 30% when the legs are retracted ($\alpha$=65°). We chose a servo motor that can generate 5.7 Nm of torque, in order to withstand the sprawl's expected loads with a safety factor (SF) of more than 2.

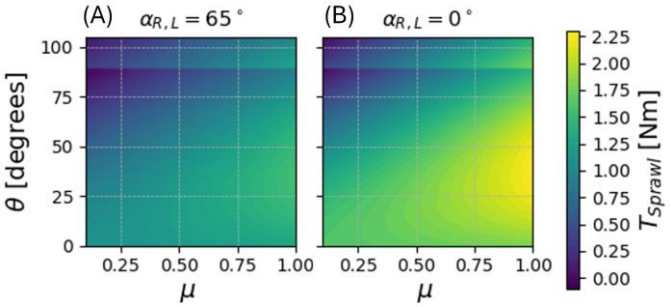


Figure 13. Sprawl torque as a function of the COF $\mu$ and sprawl angle $\theta$. (A) FBEM is at minimal extension ($\alpha_R$=$\alpha_L$=65°). (B). FBEM is at maximal extension ($\alpha_R$=$\alpha_L$=0°).

#### *2) FBEM Torque Requirements*

The torque acting on the FBEM is shown in Figure 14. The radial forces $F_{r_{R/L}}$ acting on the wheels are balanced by the FBEM actuator's extension forces $F_{FBEM_{R/L}}$. The radial force on the wheels combines normal and frictional forces, shown in Figure 12, is given by:

$$F_{r_{R/L}} = F_{N_{R/L}}\sin(\theta\pm\gamma) - f\cos(\theta\pm\gamma) \tag{14}.$$

Inserting the values of $F_{N_{R/L}}$ and $f$, we obtain:

$$F_{r_R} = mg\left(\left(1-\frac{COM_x}{W_{\text{Sprawl}}}\right)\sin(\theta+\gamma) - \mu\frac{COM_x}{W_{\text{Sprawl}}}\cos(\theta+\gamma)\right) \tag{15}$$

and

$$F_{r_L} = mg\frac{COM_x}{W_{\text{Sprawl}}}\cdot\left(sin(\theta-\gamma)-\mu cos(\theta-\gamma)\right) \quad (16).$$

By subtracting the leg's weight, the FBEM forces are:

$$F_{FBEM_{R/L}} = F_{r_{R/L}} - m_{\text{Leg}} g\, sin(\theta \pm \gamma) \quad (17)$$

Inserting the values of the forces $F_r$, we obtain:

$$F_{FBEM_R} = \left(m\left(1-\frac{COM_x}{W_{\text{Sprawl}}}\right)-m_{\text{Leg}}\right) g\, sin(\theta+\gamma)... \\ -\mu mg\frac{COM_x}{W_{\text{Sprawl}}} cos(\theta+\gamma) \quad (18)$$

and

$$F_{FBEM_L} = \left(m\cdot\frac{COM_x}{W_{\text{Sprawl}}}-m_{\text{Leg}}\right) g\, sin(\theta-\gamma)... \\ -\mu mg\frac{COM_x}{W_{\text{Sprawl}}} cos(\theta-\gamma) \quad (19).$$

Neglecting the forces acting in the fore-aft direction, the torque acting on the motor is:

$$T_{FBEM_{R/L}} = -F_{FBEM_{R/L}}\cdot L_{\text{Bar}}\, sin(\alpha_{R/L}) \quad (20).$$

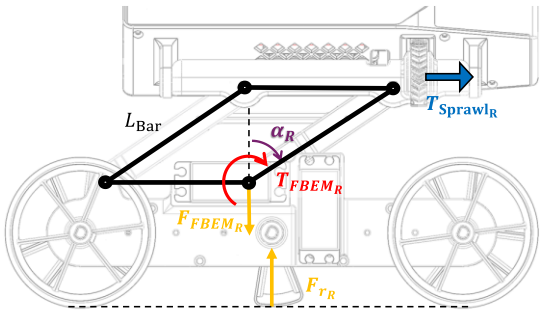


Figure 14. Forces and torque diagram in the plane of the FBEM.

Figure 15 presents the FBEM torque (produced by the servo motors) as a function of $\alpha_R$ and $\alpha_L$ for two sprawl angles $\theta$=90° and $\theta$=105°.

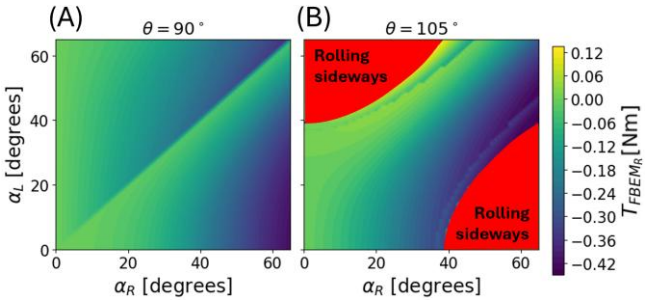


Figure 15. FBEM torque as a function of the FBEM angles for two different sprawling angles (90 and 105 degrees). The red zone presents the conditions in which the robot tips over on one side.

The figure presents the discontinuities that occur as the ground contact points shift from the inner to the outer wheels. The rolling sideways zone is calculated as in Eq. (7). Section III.D. For the FBEM mechanism, we selected servo motors rated at 2.29 Nm, providing sufficient torque to drive the FBEM with a safety factor of 5.

## IV. Results

This section presents the results of experiments conducted on the robot. We analyzed the robot's ability to advance, turn, roll, overcome different obstacles, and drive over different terrains. During the experiments, the robot was either manually controlled by a human operator or received a command to perform an automated sequence.

### A. Turtle Gait

In the first experiment, the robot moved its FBEM angle in the range $\alpha$=60° to $\alpha$=-60° while the sprawl alternated between -45° to +45°. The robot advanced by an average of 14.8 cm per cycle (average of 15 cycles) and a standard deviation of 0.16 cm. This result is within 1% of the expected result as stated in Eq. (3). By using a similar gait pattern but inverting the FBEM direction of one side (Figure 16), the robot rotated by an average of 44.1° in each cycle, which was 12% lower than the expected result (50.1°) as in Eqs. (5) and (4) (an average of 15 cycles and a standard deviation (SD) of 3.9°). The difference was likely due to sliding on the surface.

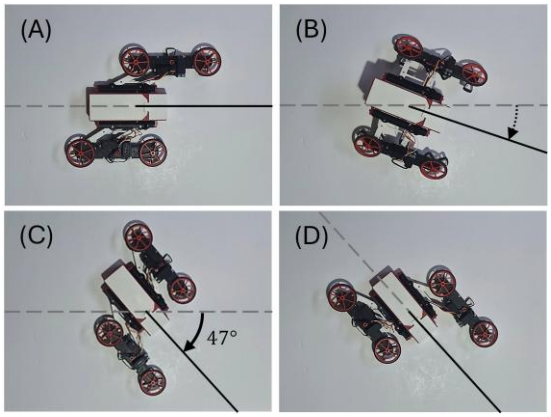


Figure 16. The robot turning while using the turtle gait. Starting in (A), the robot is moving its left leg backward and pushing its right leg forward while the sprawl is positive in order to rotate (B). Then it lifts its legs (C) to reverse leg direction to finish the cycle (D). See attached video.

### B. Rolling Sideways

The robot is able to move its COM in the lateral direction (sideways) by actuating its sprawl and FBEM mechanisms until it rolls on its side (see Figure 17).

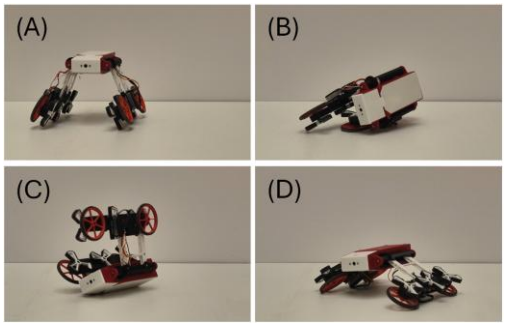


Figure 17. The robot rolling sideways. Starting in (A), The FBEM was increased on the left side while the sprawl angle was increased to beyond 90° (B). At this stage, the robot started rolling over (C) and ended on its back. In (D), the robot is shown after completing a full 180° rotation. See attached video.

The experiments, (repeated 15 times) showed similar results as predicted by our analysis in Section III.D. When maintaining the FBEM angles respectively at 0° and 65° and increasing the sprawl by steps of 5°, the robot rolled over when the sprawl reached an average of 90.3° (SD=1.3°). This result is slightly smaller than our expected result in Eq. (7). This may have been due to some backlash at the joints causing the sprawl to be slightly larger than the servo motor angle. In the next experiment, we used the max sprawl of 105° and kept one FBEM at 0° while increasing the other FBEM in steps of 5°. The flip occurred at an average of 35.0° (SD=3.9°) which also compares satisfactorily with our analysis (40°).

### *C. Traversing a Variety of Surfaces and Obstacles*

Finally, we conducted outdoor experiments on various surfaces. The robot successfully navigated rocky terrain with rocks as large as its wheels and maneuvered across grass, gravel, and flat ground (see video). Additional experiments confirmed that this method enabled the robot to overcome a wide range of obstacles, including climbing 15 cm steps (equivalent to its fully extended leg), surmounting 20 cm wall-like obstacles (about half the robot's width), crossing 18 cm long gaps, and passing through vertical openings as narrow as 10 cm. (see Figure 18).

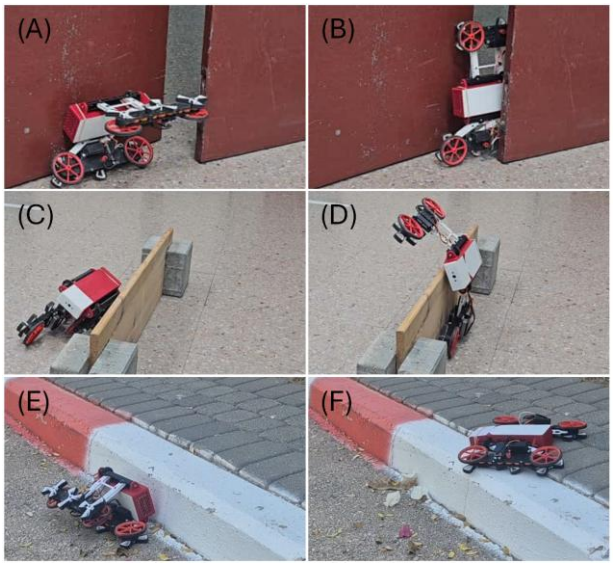


Figure 18. The robot demonstrating three different obstacle-overcoming maneuvers using rolling sideways. In (A–B), it passes through a narrow vertical gap (10 cm wide) between two doors. In (C–D), it rolls sideways over a 20 cm wall. In (E–F), it combines rolling over a 15 cm step with the turtle gait, using its legs to complete the climb and stabilize on the platform. See attached video.

## V. Conclusions

This paper presented the Decoupled STAR (DSTAR), a novel reconfigurable robot equipped with a dynamic sprawling mechanism and two independently actuated four-bar extension mechanisms (FBEM). The robot is fitted with both wheels and whegs and can transition between them. The DSTAR has high reconfigurability in that it can change its geometry and shift its COM along multiple planes. The sprawling mechanism allows sprawl angles ranging from -105° to +105° while the FBEM allows angles ranging from -65° to +65°, thus enabling the robot to perform controlled rolling maneuvers, invert its orientation, and dynamically adjust its body height and width for effective obstacle engagement. The DSTAR achieves body height variations from 24 mm to 153 mm, has a variable width from 38 mm to 403 mm, and an adjustable length ranging from 269 mm to 367 mm.

The kinematic and quasi-static analyses confirmed that rolling sideways can be reliably and repeatedly initiated at either a minimal sprawl angle of 99° using the maximal FBEM extension differences between the legs, or at a minimum FBEM angle of 40° at maximum sprawl angles. This rolling motion allows the robot to overcome obstacles and replace its wheels with its whegs or vice-versa. The results were within 12% of our theoretical expectations.

The turtle gait allows the robot to crawl over different surfaces such as grass and climb over a variety of obstacles up to 9 cm in height (see video). The robot can advance by 14.8 cm in a single "turtle cycle" (within 1% our analytical expectations) and rotate by 44.1° per cycle (within 12% of our theoretical expectations). The difference was likely due to the legs sliding during the rotation.

Compared to RSTAR, the DSTAR demonstrates significantly enhanced locomotion and obstacle engagement capabilities. It can directly climb obstacles up to 9 cm (versus RSTAR's 6 cm) and, by flipping sideways, overcome 20 cm wall obstacles and 15 cm steps which constitute improvements of 122% and 66%, respectively (while accounting for ~1.5:1 size ratio). DSTAR uniquely passes through vertical gaps (e.g., cracks or partially open doors), and it can flip slowly to change contact wheels, unlike RSTAR which required fast dynamic maneuvers. It also enables turtle-gait rotation, allowing stable navigation over long grass or smooth terrain where wheels may fail. Additionally, DSTAR can traverse slopes laterally, maintaining stability across surfaces at different heights.

TABLE II. Normalized comparison of design and locomotion metrics among STAR robots

| STAR Version | STAR | RSTAR | TSTAR | DSTAR |
|---|---|---|---|---|
| Mass [gr] | 73 | 308 | 602 | 1150 |
| Body Length (BL) [mm] | 120 | 150 | 400 | 269 |
| Wheel diameter [mm] | 56 | 54 | 60 | 76 |
| Speed [BL/s] | **5m/s 43.3** | 1m/s 6.7 | 0.38 m/s 0.9 | 0.42 m/s 1.53 |
| Gap traversal [BL] | - | - | (180 mm) 0.45 | **(180 mm) 0.66** |
| Overcoming obstacle height BL | (35 mm) 0.29 | (60 mm) 0.40 | (180 mm) 0.45 | **(200mm) 0.74** |

Independent FBEM control allows shifting the robot's center of mass (COM) sideways, enabling controlled sideways flipping to climb higher obstacles. This capability also supports horizontal traversal on slopes, applying greater contact forces for climbing gaits, quasistatic wheel changes, and even passage through 10 cm wide vertical cracks. Using an asymmetric FBEM configuration, the robot can cross an 18 cm horizontal gap.

Future research will concentrate on dynamic analyses and enhancing DSTAR's autonomy by developing Deep Reinforcement Learning (DRL) algorithms. Integrating visual and inertial sensor feedback will enable real-time adaptive decision-making, further exploiting its mechanical versatility.

## VI. References

[1] J. M. Morrey, B. Lambrecht, A. D. Horchler, R. E. Ritzmann, and R. D. Quinn, "Highly mobile and robust small quadruped robots," in *Proc. 2003 IEEE/RSJ Int. Conf. on Intelligent Robots and Systems (IROS)*, Las Vegas, NV,

USA, Oct. 2003, pp. 82–87.
[2] A. M. Hoover, S. Burden, X. Y. Fu, S. S. Sastry, and R. S. Fearing, "Bio-inspired design and dynamic maneuverability of a minimally actuated six-legged robot," in *Proc. 3rd IEEE RAS & EMBS Int. Conf. on Biomedical Robotics and Biomechatronics (BioRob)*, Tokyo, Japan, Sep. 2010, pp. 869–876.
[3] P. Birkmeyer, K. Peterson and R. S. Fearing, "DASH: A dynamic 16g hexapedal robot," *2009 IEEE/RSJ International Conference on Intelligent Robots and Systems*, St. Louis, MO, USA, 2009, pp. 2683-2689
[4] Y. S. Kim, G. P. Jung, H. Kim, K. J. Cho, and C. N. Chu, "Wheel Transformer: A wheel-leg hybrid robot with passive transformable wheels," *IEEE Trans. on Robotics*, vol. 30, no. 6, pp. 1487–1498, Dec. 2014.
[5] S. Kim, J. E. Clark, and M. R. Cutkosky, "iSprawl: Design and tuning for high-speed autonomous open-loop running," in *The International Journal of Robotics Research*, vol. 25, no. 9, pp. 903–912, Sep. 2006.
[6] R. Yun, M. Qi, Z. Liu, and J. Leng, "Modeling and testing of a fast-crawling millimeter-sized robot," *IEEE Robotics and Automation Letters*, vol. 8, pp. 5862–5869, Sep. 2023.
[7] S. Grogan, R. Pellerin, and M. Gamache, "The use of unmanned aerial vehicles and drones in search and rescue operations–a survey," in Proc. PROLOG, 2018.
[8] C. Nattero, C. T. Recchiuto, A. Sgorbissa, and R. Zaccaria, "Coverage algorithms for search and rescue with UAV drones – abstract," presented at the AIRO Workshop, XIII AI*IA Symp. on Artificial Intelligence, Pisa, Italy, Dec. 10–12, 2014.
[9] G. Bevacqua, J. Cacace, A. Finzi, and V. Lippiello, "Mixed-initiative planning and execution for multiple drones in search and rescue missions," in *Proc. 25th Int. Conf. on Automated Planning and Scheduling (ICAPS)*, Jerusalem, Israel, pp. 315–323, Jun. 2015
[10] D. Chatziparaschis, M. G. Lagoudakis, and P. Partsinevelos, "Aerial and ground robot collaboration for autonomous mapping in search and rescue missions," Drones, vol. 4, no. 4, art. 79, Dec. 2020.
[11] T. J. Allen, R. D. Quinn, R. J. Bachmann, and R. E. Ritzmann, "Abstracted biological principles applied with reduced actuation improve mobility of legged vehicles," in *Proc. 2003 IEEE/RSJ Int. Conf. on Intelligent Robots and Systems (IROS)*, Las Vegas, NV, USA, Oct. 2003.
[12] R. T. Schroer, M. J. Boggess, R. J. Bachmann, R. D. Quinn, and R. E. Ritzmann, "Comparing cockroach and Whegs robot body motions," in Proc. IEEE Int. Conf. on Robotics and Automation (ICRA), New Orleans, LA, USA, Apr.–May 2004, pp. 3288–3293.
[13] P. Zhou, S. Tang, Y. Liu, J. Zhao, and Z. Sun, "Reconfigurable wheel crawler integrated walking mechanism design and kinetic analysis," Industrial Robot: The International Journal of Robotics Research and Application, vol. 50, no. 4, pp. 633–647, Mar. 2023.
[14] X. Y. Sandoval-Castro, S. Muñoz-González, P. D. Ferrusca-Monroy, and M. F. Ruiz-Torres, "Four-bar linkage reconfigurable robotic wheel: Design, kinematic analysis, and experimental validation for adaptive size modification," *Robotica*, vol. 42, no. 6, pp. 2046–2060, Jun. 2024.
[15] G. Liang, D. Wu, Y. Tu, and T. L. Lam, "Decoding modular reconfigurable robots: A survey on mechanisms and design," *The International Journal of Robotics Research*, vol. 44, no. 5, pp. 740–767, Nov. 2024.
[16] X. Ai, H. Yue, and W. D. Wang, "Crawling soft robot exploiting wheel legs and multimodal locomotion for high terrestrial maneuverability," IEEE Trans. on Robotics, vol. 39, no. 6, pp. 4230–4239, Dec. 2023.
[17] M. B. Khan, T. Chuthong, C. D. Do, M. Thor, P. Billeschou, J. C. Larsen, and P. Manoonpong, "iCrawl: An inchworm-inspired crawling robot," IEEE Access, vol. 8, pp. 200655–200668, 2020.
[18] T. Yanagida, R. E. Mohan, T. Pathmakumar, K. Elangovan, and M. Iwase, "Design and implementation of a shape shifting rolling–crawling–wall-climbing robot," *Applied Sciences*, vol. 7, no. 4, art. 342, Mar. 2017.
[19] Q. Chang, B. Yu, H. Ji, H. Li, T. Yuan, X. Zhao, H. Ren, and J. Zhan, "Design and control of a reconfigurable robot with rolling and flying locomotion," *Actuators*, vol. 13, art. 27, Jan. 2024.
[20] Q. Wang, N. Xiang, J. Lang, B. Wang, D. Jin, and L. Zhang, "Reconfigurable liquid-bodied miniature machines: Magnetic control and microrobotic applications," *Advanced Intelligent Systems*, vol. 6, no. 2, art. 2300108, 2024.
[21] C. C. Phipps, B. E. Shores, and M. A. Minor, "Design and quasi-static locomotion analysis of the rolling disk biped hybrid robot," *IEEE Trans. on Robotics*, vol. 24, no. 6, pp. 1302–1314, Dec. 2008.
[22] A. Yamano, Y. Ikeda, K. Imai, and M. Chiba, "Efficient rolling motion for snake-like robots utilizing center of gravity shift," *Mechatronics*, vol. 85, art. 102956, Jul. 2023.
[23] J. Jiang, Y. Zhang, S. Song, and J. Sun, "Research development of centroid deviation type spherical robot," *Recent Patents on Engineering*, vol. 17, no. 2, 2023.
[24] A. Western, M. Haghshenas-Jaryani, and M. Hassanalian, "Golden wheel spider-inspired rolling robots for planetary exploration," *Acta Astronautica*, vol. 204, pp. 34–48, Mar. 2023.
[25] H. Mochiyama, E. Shimemura, and H. Kobayashi, "Shape control of manipulators with hyper degrees of freedom," *International Journal of Robotics Research*, vol. 18, no. 6, pp. 584–600, Jun. 1999.
[26] R. Siddall, T. Fukushima, D. Bardhi, B. Perteshoni, A. Morina, E. Hasimja, Y. Dujaka, G. Haziri, L. Martin, H. Banerjee, and A. Jusufi, "Compliance, mass distribution and contact forces in cursorial and scansorial locomotion with biorobotic physical models," *Advanced Robotics*, vol. 35, no. 7, pp. 437–449, 2021.
[27] D. Spitaleri, G. Pepe, and M. Laurenza, "Enhancing spherical rolling robot control for slippery terrain," in *Proc. IEEE Workshop on Robot Motion and Control (RoMoCo)*, Poznań, Poland, Jun. 2024.
[28] D. Zarrouk, A. Pullin, N. J. Kohut, and R. S. Fearing, "STAR - Sprawl Tuned Autonomous Robot", IEEE Int. Conf. on Robotics and Automation, pp. 20-25, 2013.
[29] D. Zarrouk, and L. Yehezkel, "Rising STAR: A highly reconfigurable sprawl tuned robot", IEEE Robotics and Automation letters, vol. 3, no. 3, pp. 1888-1895, 2018.
[30] M. Coronel and D. Zarrouk, "Overcoming obstacles using Tail STAR: a novel sprawling robot with a two-joint tail," *IEEE Robotics and Automation Letters*, vol. 8, no. 4, pp. 2317–2324, Apr. 2023.
[31] N. Meiri, and D. Zarrouk, "Flying star, a hybrid crawling and flying sprawl tuned robot", IEEE Int. Conf. on Robotics and Automation, pp. 5302-5308, 2019.
[32] N. Ben David, and D. Zarrouk, "Design and analysis of FCSTAR, a hybrid flying and climbing sprawl tuned robot", IEEE Robotics and Automation Letters, vol. 6, no. 4, pp. 6188-6195, 2021.
[33] A. Cohen, and D. Zarrouk, "The AmphiSTAR high speed amphibious sprawl tuned robot: Design and experiments", IEEE/RSJ Int. Conf. on Intelligent Robots and Systems, pp. 6411-6418, 2020.
[34] O. Simhon, Z. Karni, S. Berman, and D. Zarrouk, "Overcoming obstacles with a reconfigurable robot using deep reinforcement learning based on a mechanical work-energy reward function," *IEEE Access*, vol. 11, pp. 47681–47689, 2023.

## VII. APPENDIX

The position of the COM of the different robot parts relative to the ground:

$$\mathbf{C}_{\text{Body}} = \begin{pmatrix} W_W c(\theta+\gamma\pm 90) + L_{\text{Leg}_R}\, c(\theta+\gamma) + X_B c(\gamma) - Y_B s(\gamma) \\ W_W s(\theta+\gamma\pm 90) + L_{\text{Leg}_R} s(\theta+\gamma) + X_B s(\gamma) + Y_B c(\gamma) \\ d_1 - d_2 + L_{\text{Bar}}\, sin\,\alpha_R + Z_{\text{Body}} \end{pmatrix} \quad (21).$$

For brevity, we use $W_W$ instead of $W_{\text{Wheel}}$ and B instead of Body.

$$\mathbf{C}_{\text{Leg}_R} = \begin{pmatrix} -X_{\text{Leg}}\, sin(\theta+\gamma) + Y_{\text{Leg}}\, cos(\theta+\gamma) \\ -X_{\text{Leg}}\, cos(\theta+\gamma) + Y_{\text{Leg}}\, sin(\theta+\gamma) \\ Z_{\text{Leg}} \end{pmatrix} \quad (22)$$

$$\mathbf{C}_{\text{Leg}_L} = \begin{pmatrix} W_{\text{Sprawl}} + X_{\text{Leg}}\, sin(\theta-\gamma) - Y_{\text{Leg}}\, cos(\theta-\gamma) \\ X_{\text{Leg}}\, cos(\theta-\gamma) + Y_{\text{Leg}}\, sin(\theta-\gamma) \\ Z_{\text{Leg}} + L_{\text{Bar}}(sin\,\alpha_R - sin\,\alpha_L) \end{pmatrix} \quad (23).$$

For the case where the outer wheels are in contact with the ground, $\mathbf{C}_{\text{Leg}_R}$ is as follows:

$$\mathbf{C}_{\text{Leg}_R} = \begin{pmatrix} (2W_{\text{Wheel}} - X_{\text{Leg}})\, sin(\theta+\gamma) + Y_{\text{Leg}}\, cos(\theta+\gamma) \\ (2W_{\text{Wheel}} - X_{\text{Leg}})\, cos(\theta+\gamma) + Y_{\text{Leg}}\, sin(\theta+\gamma) \\ Z_{\text{Leg}} \end{pmatrix} \quad (24)$$

where $X_{\text{Leg}}$=22mm, $Y_{\text{Leg}}$=40mm, $Z_{\text{Leg}}$=-97mm, $X_{\text{Body}}$=10mm, $Y_{\text{Body}}$=-5 mm, $Z_{\text{Body}}$=-95mm.